Automated on-axis direct laser writing of coupling elements for photonic chips

EDGAR PEREZ[1,2,*], GREGORY MOILLE[1,2], XIYUAN LU[1,3], DARON WESTLY[2] AND KARTIK SRINIVASAN[1,2,*]

[1] *Joint Quantum Institute, NIST/University of Maryland, College Park, MD 20742 USA*

[2] *Physical Measurement Laboratory, National Institute of Standards and Technology, 100 Bureau Drive Gaithersburg, MD 20899 USA*

[3] *Institute for Research in Electronics and Applied Physics, University of Maryland, College Park, MD 20742 USA*

[*] *perezed@umd.edu; kartik.srinivasan@nist.gov*

Abstract: Direct laser writing (DLW) has recently been used to create versatile micro-optic structures that facilitate photonic-chip coupling, like free-form lenses, free-form mirrors, and photonic wirebonds. However, at the edges of photonic chips, the top-down/off-axis printing orientation typically used limits the size and complexity of structures and the range of materials compatible with the DLW process. To avoid these issues, we develop a DLW method in which the photonic chip's optical input/output (IO) ports are co-linear with the axis of the lithography beam (on-axis printing). Alignment automation and port identification are enabled by a 1-dimensional barcode-like pattern that is fabricated within the chip's device layer and surrounds the IO waveguides to increase their visibility. We demonstrate passive alignment to these markers using standard machine vision techniques, and print single-element elliptical lenses along an array of 42 ports with a 100 % fabrication yield. These lenses improve fiber-to-chip misalignment tolerance relative to other fiber-based coupling techniques. The 1 dB excess loss diameter increases from $\approx$ 2.25 μm when using a lensed fiber to $\approx$ 10 μm when using the DLW printed micro-optic and a cleaved fiber. The insertion loss penalty introduced by moving to this misalignment-tolerant coupling approach is limited, with an additional loss (in comparison to the lensed fiber) as small as $\approx$ 1 dB and $\approx$ 2 dB on average. Going forward, on-axis printing can accommodate a variety of multi-element free-space and guided wave coupling elements, without requiring calibration of printing dose specific to the geometry of the 3D printed structure or to the materials comprising the photonic chip. It also enables novel methods for interconnection between chips. To that end, we fabricate a proof-of-concept 3D photonic wire bond between two vertically stacked photonic chips.

1. Introduction

Nanophotonic devices created in photonic chips have ushered in significant advances in computer and data communications [1], sensing [2], nonlinear optics [3], and quantum optics [4]. Even so, efficient and robust optical coupling between on-chip devices and the outside world remains a challenging problem [5]. As the exciting applications of nanophotonic technologies continue to mature, the importance of robust and cost-effective packaging methods will become a pressing priority given that they already present a significant bottleneck in the commercialization of photonic integrated circuits (PICs) [6].

To solve the packaging problem, a wide variety of solutions for fiber-to-chip coupling [5, 6] have been studied. Of these, end-fire approaches and grating couplers have emerged as practical and commonly implemented techniques. End-fire techniques, such as the use of lensed optical fibers that easily produce a focused optical spot from a standard single mode fiber input, offer a large coupling bandwidth and ease of use, but often suffer from a high sensitivity to misalignment.

Depending on the on-chip waveguide geometry, a lensed fiber may have a 1 dB misalignment tolerance of ± 0.5 μm to $\pm 1 \mu$m [5, 6], which is difficult to satisfy using passive alignment. In contrast, grating couplers can extend this tolerance significantly, but (in general) they suffer from smaller coupling bandwidths and often require additional fabrication steps to achieve high efficiency coupling.

Recent work on Direct Laser Writing (DLW) has demonstrated that its miniaturization of linear optical elements brings added versatility to the nanophotonics platform. In seminal papers [7–9], it was shown that DLW could be used to create free-form lenses, total-internal-reflection mirrors, and photonic wirebonds that improve fiber-to-chip coupling for photonic chips. The flexibility of DLW systems even permits the creation of plug-and-play-type solutions [10, 11] and broadband out-of-plane coupling [12, 13]. Despite the tremendous progress made with DLW, its implementation is still challenging in some contexts. Specifically, this includes the ability to write structures at any depth on the chip facets, without regard to the specific materials comprising the chip, and without the need for complicated, structure-dependent simulations.

In this paper, we present a method for DLW that uses machine vision and barcode-like patterns to overcome the aforementioned fabrication challenges associated with printing micro-optic elements on chip facets (i.e., input/output (IO) ports). Section 2 describes the problem: current DLW methods have lithography beams that get obstructed when printing at the edge of the chip, reducing the size and optical quality of the printed micro-optics and limiting the materials compatible with the DLW process. To solve these issues, Section 3 proposes a new DLW method that orients photonic chips so that the lithography beam can access the IO facet of a photonic chip without obstruction. Printing from this orientation requires the labeling and detection of very small features ($\approx$ 200 nm length scale), which are problems simultaneously solved by incorporating high-visibility information-encoding barcode-like markers. Section 4 presents a machine-vision algorithm, composed of well-established image processing techniques, that reliably detects, reads, and aligns-to the barcode patterns. The utility of this DLW method and algorithm is demonstrated by fabricating micro-optic lenses along an array of waveguides. In Section 5, we describe the experimental methods used during this characterization process, and our results are presented in section 6. Future possibilities brought about by our technique are discussed in Section 7, where we fabricate a proof-of-concept photonic wirebond between vertically stacked chips. We conclude by offering some remarks on the process and its relevance to dense photonics packaging.

2. Challenges with off-axis printing

The tremendous progress made in printing micro-optic elements on the facets of photonic chips [7, 9, 14, 15] has been achieved using approaches that typically employ top-down (off-axis) printing, resulting in challenges due to the orientation of the chip with respect to the lithography beam. To describe the situation further, we consider the photonic chip schematically depicted in Fig. 1(a), where a waveguide core (shown in pink) is embedded in a lower refractive index cladding (transparent green) on top of an opaque substrate (gray). In practice, the waveguide core can be made of materials like Si, Si_3N_4, or GaAs, and the cladding is typically SiO_2. The IO ports of the waveguide employ the commonly used inverse taper geometry, which improves coupling to optical fibers by better matching the mode profile of the waveguide to that of the fiber [16, 17].

Attempting to print on the IO port of such a typical chip in the traditional manner, from the top-down (off-axis) perspective shown in Fig. 1(b), will limit the micro-optic structure in three ways. First, the size and depth of the structure is limited by the working distance of the objective. While in many cases the waveguiding layer is just a few micrometers below the chip surface, so that this is not a practical limitation, there are scenarios in which this is not the case, including 3D assemblies of chip stacks or highly integrated systems in which metallic layers associated with

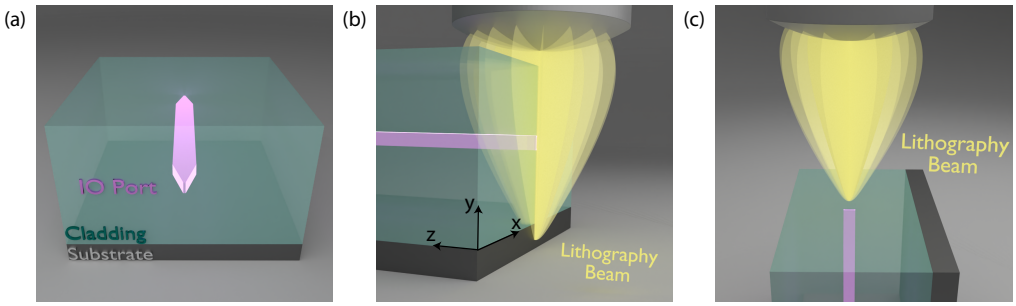

Fig. 1. Direct laser writing on the facet of a typical photonic chip can be challenging when done from the off-axis perspective. (a) A device in a typical photonic chip (not to scale) consists of a high refractive index waveguide core (shown in pink) surrounded by a lower refractive index cladding (transparent green), all on a high refractive index substrate (dark gray). The waveguide core is tapered down to a small width at the facet to create an input/output (IO) port with improved mode matching, and hence optical coupling, to a single-mode optical fiber. (b) With off-axis printing, the lithography beam from the DLW system is partially obstructed by the cladding when printing an optical structure at the chip facet, and the working distance of the objective limits the size and depth of the printable area. The influence of this obstruction becomes more significant if the cladding refractive index is larger or if reflective layers (e.g., metal) are present. (c) Flipping the chip (i.e., on-axis printing), so that the primary axis of the port is co-linear with the axis of the lithography beam prevents the beam obstruction and enables printing with an objective of any working distance, regardless of the specific material stack comprising the photonic chip.

control electronics lie above the photonics. Second, near the facet, the lithography beam will partially overlap with the chip, as shown in Fig. 1(b), causing aberrations that distort the focal point. This is known as the shadowing effect, and previous studies indicate that it can decrease the effective dose at the focal point [14] and deteriorate the quality of the focused beam [18]. It is possible to dynamically adjust the power of the beam so that the effective dose remains constant [18], but this requires dispersion simulations for each micro-optic design and still suffers from decreased focal spot quality. Finally, in the above cases it is assumed that the layers of the photonic chip are transparent at the wavelength of the lithography beam, so that the primary effect is dispersive. In practice, the photonic chip may contain reflective and absorptive layers like metallic traces or silicon layers which absorb commonly used lithography wavelengths (e.g., 780 nm). These layers would cause a significant distortion of the lithography beam and would be hard to compensate.

3. On-axis printing with barcode patterns

To circumvent the issues associated with off-axis printing, we propose writing structures in the on-axis orientation shown in Fig. 1(c), so that the IO facet of a chip is perpendicular to the lithography beam. This change in orientation removes limitations on the micro-optic size set by the working distance of the objective, avoids any obstruction of the lithography beam, and reduces the possibility of unwanted absorption/reflections since the lithography beam interacts only with the facet of the device, rather than each boundary in the layer stack. On the other hand, orienting the chip for on-axis printing introduces a new set of challenges, primarily related to the ability to image the facet well enough for high-accuracy localization of the waveguide terminations (IO ports). We note that this challenge is distinct from that faced in previous implementations of DLW in on-axis configurations, where, for example, structures have been

written on the facets of optical fibers [7, 19–23]. In such instances, injection of laser light into the fiber could enable its active alignment to the lithography beam [22], while passive alignment has also been pursued [7, 19–23]. However, passive on-axis alignment to fiber facets is a qualitatively different challenge from the one addressed here, on-axis alignment to nanophotonic waveguides, due to the critical feature sizes encountered. Whereas the core diameter of a typical single mode fiber for 1550 nm operation is $\approx 9\ \mu$m, a photonic waveguide at a chip facet may be just a couple hundred nanometers in width. Since the waveguides themselves are used as alignment features, it is significantly more challenging to align to an inversely tapered on-chip waveguide than an optical fiber. A second challenge associate with on-axis printing is the absence of traditional labels, which provide information about the device connected to a given IO port.

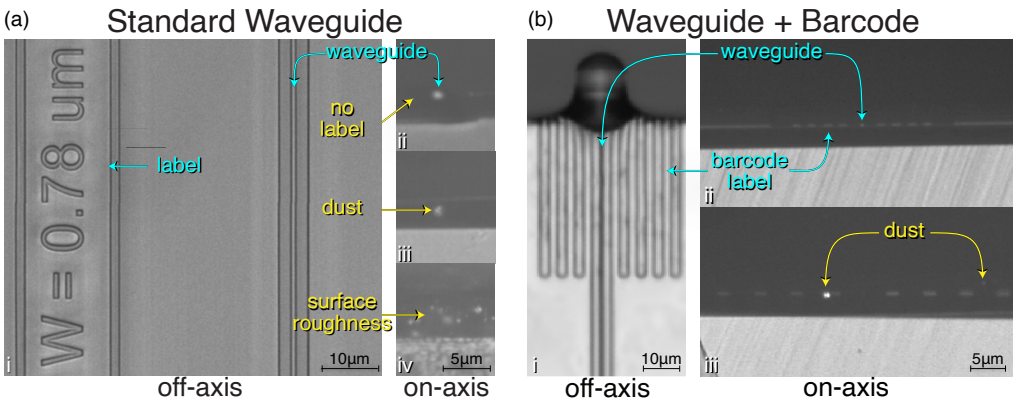

Fig. 2. A comparison between the off-axis and on-axis perspectives of viewing standard waveguides (a) and waveguides with adjacent barcode patterns (b). From the off-axis perspective (a, i), features like labels or waveguides are easily identifiable. From the on-axis perspective (a, ii-iv), only the cross section of the waveguide can be imaged, hence, the waveguide becomes a small dot (a, ii) that can be confused with dust (a, iii) or spurious reflections (a, iv) from surface imperfections. The barcode patterns in (b) provide a label that can be read from both orientations with high visibility and tolerance to surface imperfections due to its large spatial extent. While in image (b, ii) the waveguide itself is visible, in image (b, iii) it is not, and moreover strong reflections from contaminant particles are present. Nevertheless the waveguide center can be inferred after detection of the barcode elements. We note that (b, i) also displays a DLW-printed micro-lens at its facet.

To make this discussion more concrete, in Fig. 2 we present off-axis and on-axis images of a waveguide device in a photonic chip. This specific chip is comprised of a 550 nm thick silicon nitride (Si_3N_4) waveguide core surrounded by $\approx 6\ \mu$m of silicon dioxide (SiO_2) cladding ($\approx 3\ \mu$m above and below the waveguide), all on a silicon (Si) substrate. The waveguides are 1 μm wide, and are tapered down to a nominal width of 200 nm at the facet. Such a relatively thick Si_3N_4 layer is consistent with our recent demonstrations of nonlinear optical functionality in this platform [24–27]. From the off-axis perspective, the entire plane of the device layer can be clearly imaged (Fig. 2(a-b, i)), which provides easy-to-see labels and unmistakable waveguides. From the on-axis perspective (Fig. 2(a, ii-iv) and Fig. 2(b, ii-iii)), on the other hand, the information in the plane of the device layer (i.e., markers, labels, and waveguide locations) is reduced to the 1D intersection of the device layer with the edge of the photonic chip. As shown in Fig. 2(a, i) and Fig. 2(b, i), a waveguide that appears as a long line from the off-axis perspective is reduced to a small spot when viewed from the on-axis perspective (Fig. 2(a, ii)), and labels are no longer visible. Figure 2(a, ii) shows an example of an ideal situation, where the imaging/facet quality is

such that the waveguide termination at the facet is clearly visible. Such images suggest that a blob-finding algorithm could be applied to determine the waveguide center, enabling aligned lithography of a micro-optic element. However, we find that such clean images are highly sensitive to illumination conditions and can be atypical since reflections from contaminants and surface imperfections, which can be common (and dependent on facet preparation), are difficult to differentiate from the waveguide itself (Fig. 2(a, iii-iv)).

To address the visibility and information losses associated with on-axis imaging, we introduce barcode patterns (Fig. 2(b)), which transfer information from the device-layer plane to the device-layer edge while providing high-visibility markers that can be read and aligned-to from the on-axis perspective. These barcodes consist of a simple series of stripes that run parallel to the waveguide and extend all the way to the chip facet, so that they are visible when the chip is oriented in the on-axis position. The markers can encode information in the number, spacing, and width of the bars, as well as in binary encoding (bar/no bar). For example, the waveguide in Fig. 2(b, i) has a barcode consisting of three bars to the left and four bars to the right of the waveguide, but all the bars are of equal width. Furthermore, the cross-section of the markers, viewed on-axis in Fig. 2(b, ii-iii), is large enough to reduce sensitivity to spurious reflections. Moreover, even if the waveguide is itself not easily imaged, the barcode pattern is, and the waveguide center can be inferred from the location of the barcode elements. It is important to note that the barcode stripes have sufficient separation from the IO waveguide ($\approx 2\ \mu$m on each side) to avoid deterioration of its optical mode or undesired coupling to slab modes.

4. Machine vision using barcode patterns

A high-visibility barcode like that in Fig. 3(a) signals the location of a waveguide in a way that cannot be disturbed by random dust or surface impurities, given its unique signature that can be readily detected. In general, the quality of the image that the DLW system captures depends on the cleanliness of the device, the surface roughness, and the index contrast between the waveguide core material and the cladding material. We found that Si_3N_4 (refractive index $n \approx 2$) buried in SiO_2 cladding ($n \approx 1.5$) provides a sufficient index contrast for pattern localization, and we expect the image quality to improve with higher-contrast waveguides, such as Si in SiO_2.

To use the barcode pattern for waveguide identification and localization, we use well-established machine vision techniques. The algorithm developed in this work consists of several steps including a Canny filter, a Hough transform, a binary template, and a cross correlation; together, this enables alignment without coupling a visible laser through the waveguide *in-situ* (i.e., without active alignment). A step-by-step description of the algorithm is as follows. First, a medium-to-high contrast image like that shown in Fig. 3(a) is captured. Because of the long spatial extent of the barcode, medium contrast is sufficient, but high contrast is preferred. Second, a Canny filter detects edges by searching for the peaks in the gradient of the 2D image. Its output (Fig. 3(b)) consists of a binary map of edge points that are then used to compute the Hough transform of the image. The Hough transform identifies the location of straight lines, not just edges, in the binary map and determines their angles with respect to the horizontal axis of the image. This information is used to determine the location of the interface between the Si and SiO_2 layers, and its angle (θ) shown in Fig. 3(c). At this point, the information encoded in the barcode can be retrieved from a 1D line-scan of the code, whose position is determined by interpolating between the top and bottom edges of the Si_3N_4 device layer. The extracted angle θ is then applied to a binary template (Fig. 3(d)) so that the template and the original image overlay at the same angle. Finally, the template and the image are cross correlated (Fig. 3(e)), and a sub-pixel peak-search determines the position of the waveguide, depicted as the center of a small red circle in the figure. It is important to note here that neither the line-scans nor the templates assume the presence of the waveguide itself (i.e., there is no small dot at the center of the template), meaning that even in cases of low waveguide-visibility, the barcode pattern is

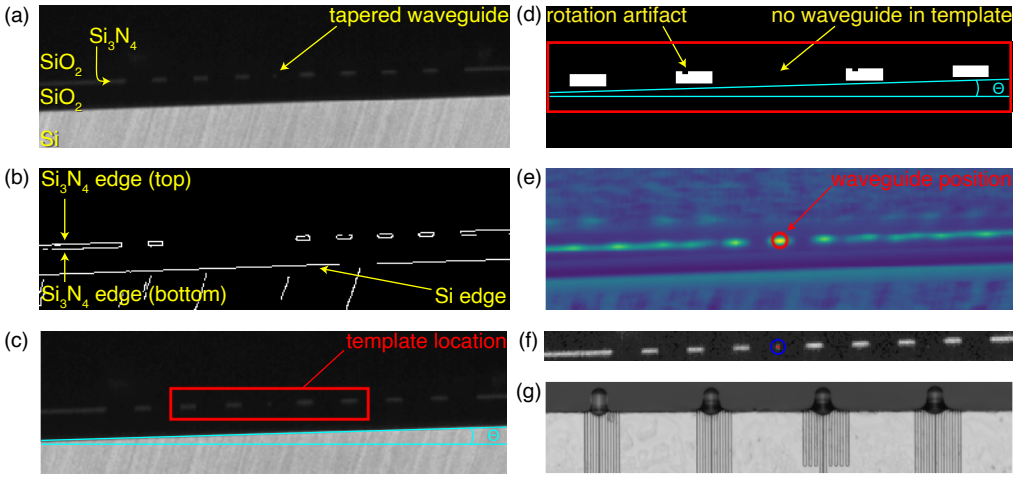

Fig. 3. Standard machine vision techniques can use a barcode pattern to determine the waveguide center more reliably than if the barcode is absent, even when subject to imaging/facet imperfections. (a) A typical image from a DLW system, with a clearly-visible barcode pattern and a tapered Si_3N_4 waveguide at its center. The contrast in the image is determined by the index contrast between the various materials and the illumination conditions. (b) The uninterrupted high-contrast edge between the underlying SiO_2 and Si layers can be easily seen in the binary output of a Canny edge detection algorithm. A Hough transform is then used to identify the straight lines from the Si-SiO_2 and Si_3N_4-SiO_2 edges in the Canny image. The detection of the Si-SiO_2 edge and its angle θ with respect to horizontal is overlaid on the original image in panel (c). Barcodes are read by taking a 1D line scan along the average of the top and bottom Si_3N_4-SiO_2 edges. The red rectangle in (c) identifies a region of interest that will be further processed using a pre-generated binary template (d) that matches said region (the tapered waveguide itself is omitted from the template, since its presence in the original image is not assured, e.g., if imaging conditions are poor). The template is rotated by the same angle θ extracted from the Si-SiO_2 line. A sub-pixel peak search in the cross correlation (e) between the original image (a) and the adjusted binary pattern (d) determines the center of the waveguide (red circle in (e)). Note that the final output of the algorithm (f) determines the location of the waveguide (red circle), but neither the edge detection, nor the cross correlation, assume the presence of a waveguide signal - only of a barcode signal. (g) Top view (off-axis) optical microscope image of four lenses printed on the facet of waveguides surrounded by the barcode pattern.

sufficient to determine the precise location of the small (200 nm wide) tapered-down waveguide termination. Figure 3(f) overlays the output of this algorithm (red and blue circles centered about the detected waveguide position) is superimposed on the original image, and shows that the waveguide location determined by machine vision is consistent with the position one could derive directly if they had a high-visibility image of the waveguide at the facet. Application of this localization algorithm to adjacent waveguides (with a micro-lens printing step after each localization) results in the array of devices shown in Fig. 3(g).

5. Experiment

The algorithm described above was implemented in the Python programming language [28], using the NumPy [29], and scikit-image [30] open-source libraries. We did not aim to optimize the computational speed of the algorithm presented. Different Python packages or other programming

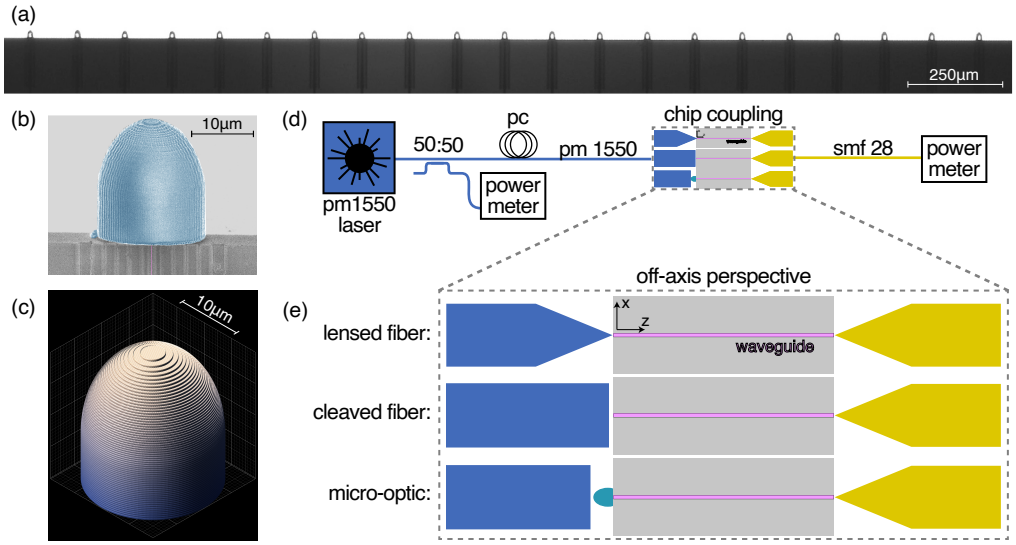

Fig. 4. Using the on-axis algorithm, arrays of micro-optic structures well-aligned to on-chip waveguides are printed with high yield. To demonstrate the utility of this technique, elliptical lenses were printed at the input facet of photonic chips, with an optical microscope image of twenty-one such lenses shown in (a). A scanning electron microscope image of one representative lens is shown in (b), with the Si_3N_4 IO waveguide's location in the plane of the chip is highlighted in pink (the Si_3N_4 is located underneath 3μm of the highlighted SiO_2), and the lens highlighted in blue. The nominal design of the lens is shown in (c). The fiber-to-chip coupling performance of the lenses was characterized using the experimental set-up shown in (d), where a 1550 nm fiber-coupled laser with polarization control (pc) is optimally-coupled to the chip via one of three fiber-based methods: lensed fibers, cleaved fibers, and cleaved fibers with micro-optics on the facet of the chip (referred to as "micro-optic method"). A zoom-in of the coupling section for the three methods is shown in panel (e). The output is collected through a lensed SMF-28e fiber in each case. Once optimally coupled, the insertion losses are measured, and the coupling sensitivity to misalignment is assessed by displacing the input fiber in the x and y directions to create excess-loss profiles. We define TE polarization as having its electric field pointing along the x-axis. pm = polarization-maintaining.

languages might provide better performance, but that is beyond the scope of this work. Even so, our localization technique only takes about two minutes to detect each waveguide. The printing process is executed on a port-by-port basis, meaning that a port is detected, aligned to, and printed on before the next port is analyzed. The algorithm can be applied successively to check for errors, since a second execution should determine that no more adjustments in position are needed. Visual inspection revealed that the algorithm was able to successfully locate, align to, and print lenses on 42 out of 42 IO waveguides, on a single chip, from the on-axis perspective (100 % fabrication yield). Twenty-one of these lenses are shown in Fig. 4(a). After localization, each lens took approximately 20 seconds to polymerize from IP-Dip photoresist [31]. About half of the write time was occupied by the auto focus procedure of the DLW system (Nanoscribe GmbH) [31]. For more details on the lithography process see Appendix A. The geometric accuracy of the lenses was verified using scanning electron microscope imaging (SEM). A representative SEM image of one of the lenses is shown in Fig. 4(b). Note that the lens (blue) is well aligned to the IO waveguide (pink). For comparison, the model of our design is illustrated in Fig. 4(c). From

these figures it is evident that the produced lens closely resembles the model.

The accuracy of the alignment is limited by the mechanical stability and imaging resolution of the DLW system. For example, repeatedly using the autofocus function of the DLW system returned slightly different values for the focal point, and leaving the system alone for periods of several minutes caused the mechanical stages to drift. Since the micro-optic structures in this study printed in 20 seconds or less, the errors due to the slow drift can be neglected. As DLW systems become increasingly sophisticated, we expect these errors to shrink. Depending on the application, it may also be possible to design micro-optics that are tolerant to miscalculation of the focal plane.

On a second chip, ten waveguides were selected, with no particular pre-screening, to verify that the on-axis printing method was not introducing unexpected errors in either the DLW process or the micro-optics themselves. Lenses that decrease the sensitivity of fiber-to-chip coupling to fiber misalignment have been demonstrated before [7, 14], and were thus chosen as an example application to benchmark the fidelity of our on-axis machine-aligned DLW process. The coupling efficiency into each waveguide and its sensitivity to misalignment was measured using the set-up shown in Fig. 4(d), where a 1550 nm (polarization maintaining) fiber-coupled laser was coupled into the on-chip waveguides using the three methods highlighted in Fig. 4(e). The lensed fiber method is a commonly used end-fire technique [5] due to its ability to realize low insertion losses because of the small focused spot size it achieves ($\approx$2.5 μm mode field diameter) and its natural compatibility with single mode optical fiber. However, it suffers from a high sensitivity to misalignment, precisely because of the small size of this focused spot, as well as the small size of the mode at the optical waveguide facet. The cleaved fiber method increases the mode field diameter (MFD) of the input fiber (nominally to $\approx$ 10.5 μm), so this method is expected to have a greater misalignment tolerance, but also greater insertion losses due to the mode-size mismatch between the fiber and the on-chip waveguide. The micro-optic method attempts to bridge these extremes by using an elliptical lens as an intermediary mode-size converter. In effect, this transfers the mode overlap problem from fiber-to-chip to micro-optic-to-chip, with the latter benefiting from the high positioning resolution of the DLW system and the permanent adhesion of the micro-optic to the chip.

Each of the ten waveguides was tested with the three coupling methods in both the TE and TM polarizations, where TE (TM) polarization is defined as having the electric field pointed along the x (y) axis of the device facet, based on the coordinate system shown in Fig. 1(b) and Fig. 4. Measurements included two-dimensional excess-loss profiles created by displacing the input fiber along the x and y directions in steps of dx and dy.

The micro-optic structures selected for this examination were elliptical lenses with minor radii of 9.3 μm and focal lengths of 20 μm. For more information on the design of the lenses, see Appendix B. As noted earlier, the Si_3N_4 waveguides are 550 nm thick, tapered down to a 200 nm width at the chip facet, and have a nominal mode field diameter of 2.5 μm. The facets in this study were created by dicing and polishing, with a nominal surface roughness of 100 nm. Away from the facet, the waveguides are 1 μm wide to reduce propagation losses.

6. Results

Figure 5(a) shows the excess loss profiles for the TE and TM polarizations (averaged across all ten waveguides) of the micro-optic coupling method with displacement steps $dx = dy = 0.5$ μm. The dashed white lines in the figure correspond to the -1 dB and -3 dB contours, which are smooth and circular – as expected due to the axial symmetry of elliptical lenses. The excess loss profiles are normalized with respect to the averaged peak efficiency of the coupling method, the explicit values of which are listed in the scatter plots of Fig. 5(c).

To make a comparison between the three coupling techniques, Fig. 5(b) shows line-scans along the x and y axes for each configuration. In this image the light-colored markers correspond

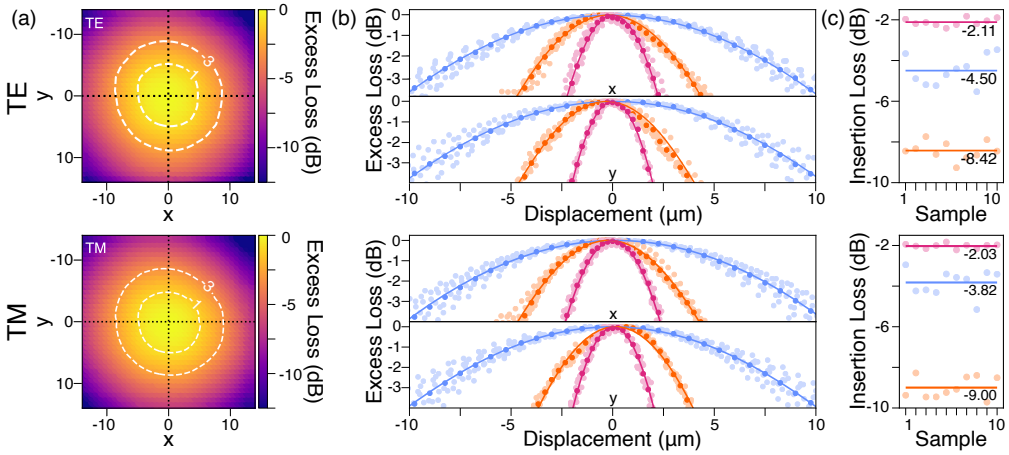

(d)

Method	TE D_{1dB}	TE D_{3dB}	TM D_{1dB}	TM D_{3dB}
Micro Optic	(9.76 ± 0.74) μm	(16.93 ± 1.30) μm	(10.00 ± 0.89) μm	(17.34 ± 1.55) μm
Cleaved Fiber	(4.19 ± 0.11) μm	(7.28 ± 0.19) μm	(4.02 ± 0.32) μm	(6.97 ± 0.55) μm
Lensed Fiber	(2.23 ± 0.14) μm	(3.87 ± 0.23) μm	(2.31 ± 0.08) μm	(4.01 ± 0.14) μm

Fig. 5. The misalignment tolerance and insertion loss of the micro-optic coupling approach is measured and compared against other end-fire coupling options. Two-dimensional maps of the excess losses were generated for each of the three cases shown in Fig. 4(c), with each case averaged across 10 waveguides. The excess loss maps (TE and TM polarizations) for the case of the micro-optic (a) show smooth, circular profiles, as expected from axially-symmetric lenses. White dashed lines on the maps indicate the -1 dB and -3 dB contours, and black dashed lines indicate the location of x and y line-scans (b) used to compare the three coupling techniques. The top (bottom) two line scan plots correspond to data from the TE (TM) polarization, in which the electric field points in the x (y) direction. Light-colored markers indicate data from the ten waveguides, dark-colored markers correspond to averages of the data, and dark-colored lines correspond to Gaussian fits of the averaged data. These line-scans show that the micro-optic approach has the greatest misalignment tolerance. Measurements of the per-facet insertion losses (c) show that the micro-optic method has on average ≈ 2 dB more loss than lensed fibers. However, the 1 dB and 3 dB diameters (d) for the micro-optic method are around four times greater for the micro-optic technique than they are for the lensed-fiber technique.

to the data from the ten waveguides, and the dark-colored markers correspond to averages of the data. The dark-colored lines correspond to Gaussian fits of the averaged data. The data show the expected trend: coupling methods that overlap large optical modes are more tolerant to displacement, and the micro-optic method (in which the fiber and lens both have large modes) has the greatest amount of displacement tolerance. This trend is quantified in Fig. 5(d), where the -1 dB and -3 dB diameters are reported. The uncertainty in these measurements is the standard deviation of the diameters about their average, and the leading source of measurement error is laser power fluctuations while the leading source of variation from waveguide to waveguide is likely the lens quality.

The insertion loss (Fig. 5(c)) for each coupling technique was measured for each of the ten waveguides in both polarizations, where we have assumed that all losses are due to facet coupling. From initial calculations, we expected the micro-optic method (blue) to perform on par with

the lensed fiber method (pink), but in practice we found that the micro-optics introduced an insertion loss penalty as small as ≈1 dB and ≈2 dB on average. 3D FDTD simulations show that errors in the micro-optic placement would need to be at the 1 μm level (far greater than the maximum placement error we observe experimentally (e.g., Fig. 4(b)) to account for the discrepancy between measured and simulated insertion losses. We believe that the added loss is likely due to imperfections in the lens fabrication, resulting from an un-optimized lithography process. For the specific DLW system we use, a transition from the current fast printing mode to a slower printing mode is expected to come with an improvement in micro-optic surface quality.

7. Discussion and future Directions: chip-to-chip interconnects

Going forward, the on-axis printing method's ability to read barcode patterns and thereby align to waveguides from the on-axis perspective opens up the possibility for novel configurations in chip-to-chip interconnects. While photonic wire bonding has achieved great success in realizing low loss interconnection between laterally adjacent photonic chips [8], one can imagine scenarios in which lateral footprint is limited, and stacks of chips may be desirable. For example, consider the stack of two chips shown in Fig. 6. In that case Chip B is identical to Chip A (besides its upside down orientation) but this need not be the case; the chips could be composed of completely different layer stacks. Such chip stacking might be useful for increasing the density of photonic devices or for combining the properties of otherwise incompatible materials. One possible solution would be to make a chip-to-chip interconnect that utilizes the barcode patterns in each chip (Fig. 6(a)) to link a specific waveguide in Chip A to a specific waveguide in Chip B. Since the methodology that we have developed above is suitable for such an endeavor, we fabricated a proof-of-concept interconnect (Fig. 6(b)) that connects a Si_3N_4 IO port from one of the chips to that in the other. In this case, the chips were bonded to each other using SU-8 [31] photoresist and the two-chip stack was transferred to the DLW system as a pre-assembled unit. Since the interconnect was fabricated using on-axis lithography, no significant modifications to the methods outlined in the previous sections were needed. We would like to emphasize that the design of the interconnect shown Fig. 6 is not suitable for low loss interconnection, but was designed so that all of the features of the 2-chip stack could be captured in one image. In practice, the bending radius should be greatly increased by laterally displacing the waveguides to be connected, or adding a thick layer of photoresist between the two chips. With these practical concerns related to loss addressed, the interconnect can then be designed to control for properties like polarization and mode shape [32]. In contrast, any such a stack of chips would be hard to address through off-axis lithography, as both the distance between the waveguide layers and the top surface (> 500 μm, exceeding the objective working distance) as well as the absorption of the lithography beam by the top silicon substrate would be significant obstacles.

8. Conclusions

We have demonstrated that on-axis DLW can circumvent many of the issues associated with the printing of micro-optics on chip facets, including beam obstruction (the shadowing effect) and material incompatibilities. To enable high-accuracy localization of the waveguide ports, we implemented barcode-like markers (in the device layer) that can be read from the on-axis perspective. The barcodes were read and aligned-to using well-established image processing tools. As an example application of on-axis DLW, we printed an array of elliptical lenses that improve fiber-to-chip misalignment tolerance. To demonstrate some unique capabilities of on-axis printing, we fabricated a proof-of-concept 3-dimensional photonic wirebond to bridge optical ports on vertically stacked chips - a task incompatible with off-axis DLW.

As the wide-scale implementation of nanophotonic devices grows within and beyond the laboratory, the importance of dense integration and flexible packaging solutions will continue

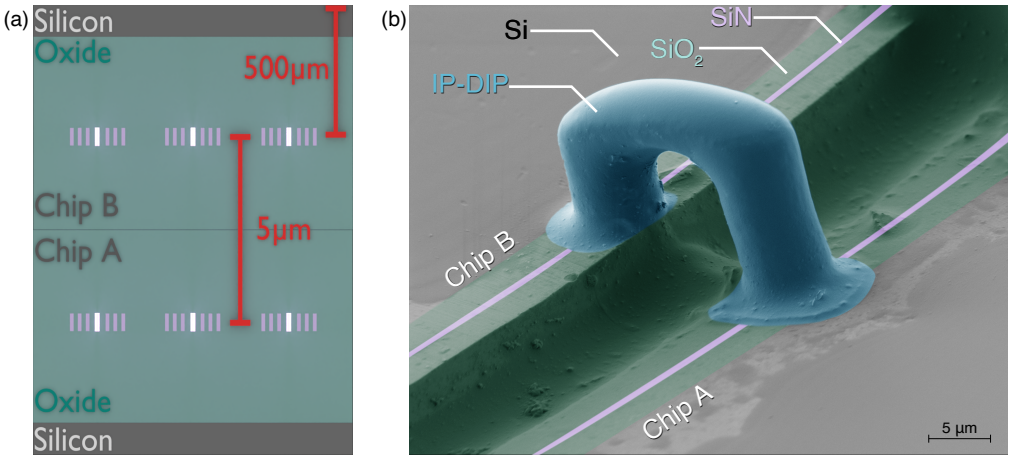

Fig. 6. On-axis direct laser writing enables novel chip-to-chip interconnects. For example, consider stacking two photonic chips as shown in (a). Printing at the edge of this system would be very challenging in the off-axis orientation because the top Si substrate is highly absorbing at the wavelength of our lithography beam (780 nm) and is thicker than the working distance of the objective. Using on-axis printing and the algorithm described in this paper, a proof-of-concept 3D chip-to-chip photonic wirebond was created using barcode patterns in each waveguide layer for alignment (b).

to grow. In fact, for the types of devices that we have described in this work (thick silicon nitride waveguides in SiO_2 cladding), there has already been progress made towards using nonlinear nanophotonics beyond the laboratory [33,34], with additional metrological applications in which the silicon nitride chip plays a central role as part of a multi-chip assembly also being developed [35,36]. We expect on-axis direct laser writing to aid in such endeavors by opening up new possibilities for robust and high-density device packaging and photonic integration.

9. Funding

The author acknowledges support from the NIST-on-a-chip and DARPA DODOS and ACES programs. X.L. acknowledges support under the Cooperative Research Agreement between the University of Maryland and NIST-PML, Award no. 70NANB10H193.

10. Disclosures

The authors have filed an invention disclosure related to the methods described in this work.

Appendix A: Fabrication

All of the lenses in this study were printed using Nanoscribe GmbH's commercial DLW system configured with a 63x objective with a 1.4 numerical aperture [31]. The system was operated in the Dip-in Laser Lithography (DiLL) mode to print on the facet of the chip, and only reflective illumination was used. The system uses a 780 nm femtosecond laser (Toptica, FemtroFiber pro NIR) as its source, which is rastered with a speed of 10 mm/s, repetition rate of 80 MHz, and with an average power of 20 mW entering the aperture of the objective. The raster distance between subsequent lines and between subsequent layers were set to 200 nm and 300 nm respectively. The system was operated locally (i.e., not in server mode), although server mode could be used as well.

IP-Dip was the photoresist used in this study, due to its physical and optical properties being well reported in the literature [7, 37–40], and its frequent use with the DLW parameters we describe in the previous paragraph. In particular references [39, 41] report losses of 0.78 dB/mm at 1550 nm through IP-Dip. Given that the typical length of our lenses was approximately 20 μm, this corresponds to approximately 0.02 dB additional losses due to the absorption of laser light by the resist. This supports the claim that the primary loss mechanism is scattering and aberrations due to imperfections of the lens shape and surface roughness. We emphasize that the lenses in this work were made to benchmark the on-axis fabrication method, and that further recipe development could lead to improved surface quality.

In order to hold the samples in the correct orientation for on-axis DLW, as described in the main text, a custom sample mount was made. The mount is a large rectangular sheet, approximately 6 mm thick, with a cutout near the middle, at the default location of the Nanoscribe's objective. Our approximately 6 mm long chips are then laid against the walls of this cutout, with the bottom substrate of the chip in contact with the wall and held in place with a nylon-tipped setscrew. This type of mount would not work with air-clad devices, but other mounts could be designed for that purpose. This type of mount was easy to fabricate and held the samples securely in place.

Appendix B: Lens Design Details

The lenses in this study are axially symmetric ellipsoids with minor diameters of 18.6 μm and focal lengths of 20 μm. An ellipse was chosen because of its ability to focus light of a single wavelength without spherical aberrations. To increase adhesion between the lens and the surface of the photonic chip, the bottom half of the ellipse was embedded in a cylinder of the same radius. This ellipse-with-cylindrical-base geometry is what gives the lenses in Fig. 4(b-c) their bullet-like shape. The exact equation for the curve of our ellipse is $\rho(z) = \sqrt{(r/\beta - \gamma z)^2 - (r/\beta - z)^2}$ where $r = 9.3$ μm is the design's minor radius, z is the distance away from the apex of the ellipse in microns, $\gamma = n_{air}/n_{resist}$, $n_{air} = 1.00029$ is the index of refraction of air, $n_{resist} = 1.48922$ is the index of refraction of IP-Dip as calculated from the Cauchy coefficients measured in Ref. [37], and $\beta = 0.443166$ is a constant defined by $\beta = \sqrt{(1-\gamma)/(1+\gamma)}$. Using r as a free parameter, 3D FDTD simulations were used to optimize r for the 200 nm width inverse tapers at the IO facet of our chips. After the fabrication of the lenses, Ref. [39] reported Sellmeier coefficients for IP-Dip that calculate a refractive index for IP-Dip of 1.532 at 1550 nm. Future lens designs with IP-Dip should use the Sellmeier coefficients because they are more accurate at a greater number of wavelengths, especially those in the near-infrared [39].

References

1. Y. Vlasov, "Silicon CMOS-integrated nano-photonics for computer and data communications beyond 100G," IEEE Commun. Mag. **50**, s67–s72 (2012).
2. M. Estevez, M. Alvarez, and L. Lechuga, "Integrated optical devices for lab-on-a-chip biosensing applications: Integrated optical biosensors," Laser & Photonics Rev. **6**, 463–487 (2012).
3. A. L. Gaeta, M. Lipson, and T. J. Kippenberg, "Photonic-chip-based frequency combs," Nat. Photonics **13**, 158–169 (2019).
4. A. W. Elshaari, W. Pernice, K. Srinivasan, O. Benson, and V. Zwiller, "Hybrid integrated quantum photonic circuits," Nat. Photonics **14**, 285–298 (2020).
5. G. Son, S. Han, J. Park, K. Kwon, and K. Yu, "High-efficiency broadband light coupling between optical fibers and photonic integrated circuits," Nanophotonics **7**, 1845–1864 (2018).
6. L. Carroll, J.-S. Lee, C. Scarcella, K. Gradkowski, M. Duperron, H. Lu, Y. Zhao, C. Eason, P. Morrissey, M. Rensing, S. Collins, H. Hwang, and P. O'Brien, "Photonic Packaging: Transforming Silicon Photonic Integrated Circuits into Photonic Devices," Appl. Sci. **6**, 426 (2016).
7. P.-I. Dietrich, M. Blaicher, I. Reuter, M. Billah, T. Hoose, A. Hofmann, C. Caer, R. Dangel, B. Offrein, U. Troppenz, M. Moehrle, W. Freude, and C. Koos, "In situ 3D nanoprinting of free-form coupling elements for hybrid photonic integration," Nat. Photonics **12**, 241–247 (2018).
8. M. R. Billah, M. Blaicher, T. Hoose, P.-I. Dietrich, P. Marin-Palomo, N. Lindenmann, A. Nesic, A. Hofmann, U. Troppenz, M. Moehrle, S. Randel, W. Freude, and C. Koos, "Hybrid integration of silicon photonics circuits and InP lasers by photonic wire bonding," Optica **5**, 876 (2018).

9. N. Lindenmann, S. Dottermusch, M. L. Goedecke, T. Hoose, M. R. Billah, T. P. Onanuga, A. Hofmann, W. Freude, and C. Koos, "Connecting silicon photonic circuits to multicore fibers by photonic wire bonding," J. Light. Technol. **33**, 755–760 (2015).
10. A. Bogucki, L. Zinkiewicz, W. Pacuski, P. Wasylczyk, and P. Kossacki, "Optical fiber micro-connector with nanometer positioning precision for rapid prototyping of photonic devices," Opt. Express **26**, 11513 (2018).
11. O. A. J. Gordillo, S. Chaitanya, Y.-C. Chang, U. D. Dave, A. Mohanty, and M. Lipson, "Plug-and-play fiber to waveguide connector," Opt. Express **27**, 20305–20310 (2019). Publisher: Optical Society of America.
12. H. Gehring, A. Eich, C. Schuck, and W. H. P. Pernice, "Broadband out-of-plane coupling at visible wavelengths," Opt. Lett. **44**, 5089–5092 (2019).
13. H. Gehring, M. Blaicher, W. Hartmann, P. Varytis, K. Busch, M. Wegener, and W. H. P. Pernice, "Low-loss fiber-to-chip couplers with ultrawide optical bandwidth," APL Photonics **4**, 010801 (2019). Publisher: American Institute of Physics.
14. R. Thomas, J. Li, S. Ladak, D. Barrow, and P. M. Smowton, "In situ fabricated 3D micro-lenses for photonic integrated circuits," Opt. Express **26**, 13436 (2018).
15. Z.-N. Tian, L.-J. Wang, Q.-D. Chen, T. Jiang, L. Qin, L.-J. Wang, and H.-B. Sun, "Beam shaping of edge-emitting diode lasers using a single double-axial hyperboloidal micro-lens," Opt. Lett. **38**, 5414–5417 (2013). Publisher: Optical Society of America.
16. T. Shoji, T. Tsuchizawa, T. Watanabe, K. Yamada, and H. Morita, "Low loss mode size converter from 0.3 μm square Si wire waveguides to singlemode fibres," Electron. Lett. **38**, 2 (2002).
17. V. R. Almeida, R. R. Panepucci, and M. Lipson, "Nanotaper for compact mode conversion," Opt. Lett. **28**, 1302–1304 (2003).
18. N. Lindenmann, "Photonic Wire Bonding as a Novel Technology for Photonic Chip Interfaces," Ph.D. thesis, Karlsruher Institut für Technologie (KIT) (2017).
19. C. Liberale, G. Cojoc, P. Candeloro, G. Das, F. Gentile, F. De Angelis, and E. Di Fabrizio, "Micro-Optics Fabrication on Top of Optical Fibers Using Two-Photon Lithography," IEEE Photonics Technol. Lett. **22**, 474–476 (2010).
20. H. E. Williams, D. J. Freppon, S. M. Kuebler, R. C. Rumpf, and M. A. Melino, "Fabrication of three-dimensional micro-photonic structures on the tip of optical fibers using SU-8," Opt. Express **19**, 22910–22922 (2011).
21. T. Gissibl, S. Thiele, A. Herkommer, and H. Giessen, "Sub-micrometre accurate free-form optics by three-dimensional printing on single-mode fibres," Nat. Commun. **7**, 11763 (2016).
22. I. Weiss and D. M. Marom, "Direct 3D nano-printing on optical fiber tip," in *2015 International Conference on Optical MEMS and Nanophotonics (OMN),* (2015).
23. A. Bertoncini, V. P. Rajamanickam, and C. Liberale, "On-fiber 3D printing of photonic crystal fiber tapers for mode field diameter conversion," in *2017 Conference on Lasers and Electro-Optics Europe & European Quantum Electronics Conference (CLEO/Europe-EQEC),* (IEEE, Munich, 2017), pp. 1–1.
24. Q. Li, M. Davanço, and K. Srinivasan, "Efficient and low-noise single-photon-level frequency conversion interfaces using silicon nanophotonics," Nat. Photonics **10**, 406–414 (2016).
25. Q. Li, T. C. Briles, D. A. Westly, T. E. Drake, J. R. Stone, B. R. Ilic, S. A. Diddams, S. B. Papp, and K. Srinivasan, "Stably accessing octave-spanning microresonator frequency combs in the soliton regime," Optica **4**, 193 (2017).
26. D. R. Carlson, D. D. Hickstein, A. Lind, J. B. Olson, R. W. Fox, R. C. Brown, A. D. Ludlow, Q. Li, D. Westly, H. Leopardi, T. M. Fortier, K. Srinivasan, S. A. Diddams, and S. B. Papp, "Photonic-Chip Supercontinuum with Tailored Spectra for Counting Optical Frequencies," Phys. Rev. Appl. **8** (2017).
27. X. Lu, G. Moille, Q. Li, D. A. Westly, A. Rao, S.-P. Yu, T. C. Briles, S. B. Papp, and K. Srinivasan, "Efficient telecom-to-visible spectral translation using silicon nanophotonics," Nat. Photon. **13**, 593–601 (2019).
28. G. Van Rossum and F. L. Drake Jr, *Python tutorial* (Centrum voor Wiskunde en Informatica Amsterdam, The Netherlands, 1995).
29. T. Oliphant, "NumPy: A guide to NumPy," USA: Trelgol Publishing (2006–). [Online; accessed <today>].
30. S. van der Walt, J. L. Schönberger, J. Nunez-Iglesias, F. Boulogne, J. D. Warner, N. Yager, E. Gouillart, T. Yu, and the scikit-image contributors, "scikit-image: image processing in Python," PeerJ **2**, e453 (2014).
31. Certain commercial products or names are identified to foster understanding. Such identification does not constitute recommendation or endorsement by the National Institute of Standards and Technology, nor is it intended to imply that the products or names identified are necessarily the best available for the purpose.
32. M. Schumann, T. Bückmann, N. Gruhler, M. Wegener, and W. Pernice, "Hybrid 2D–3D optical devices for integrated optics by direct laser writing," Light. Sci. & Appl. **3**, e175–e175 (2014).
33. P. Manurkar, E. F. Perez, D. D. Hickstein, D. R. Carlson, J. Chiles, D. A. Westly, E. Baumann, S. A. Diddams, N. R. Newbury, K. Srinivasan, S. B. Papp, and I. Coddington, "Fully self-referenced frequency comb consuming 5 watts of electrical power," OSA Continuum **1**, 274–282 (2018). Publisher: Optical Society of America.
34. E. Baumann, E. V. Hoenig, E. F. Perez, G. M. Colacion, F. R. Giorgetta, K. C. Cossel, G. Ycas, D. R. Carlson, D. D. Hickstein, K. Srinivasan, S. B. Papp, N. R. Newbury, and I. Coddington, "Dual-comb spectroscopy with tailored spectral broadening in Si_3N_4 nanophotonics," Opt. Express **27**, 11869–11876 (2019). Publisher: Optical Society of America.
35. D. T. Spencer, T. Drake, T. C. Briles, J. Stone, L. C. Sinclair, C. Fredrick, Q. Li, D. Westly, B. R. Ilic, A. Bluestone, N. Volet, T. Komljenovic, L. Chang, S. H. Lee, D. Y. Oh, M.-G. Suh, K. Y. Yang, M. H. P. Pfeiffer, T. J. Kippenberg, E. Norberg, L. Theogarajan, K. Vahala, N. R. Newbury, K. Srinivasan, J. E. Bowers, S. A. Diddams, and S. B. Papp,

"An optical-frequency synthesizer using integrated photonics," Nature **557**, 81–85 (2018).
36. Z. L. Newman, V. Maurice, T. Drake, J. R. Stone, T. C. Briles, D. T. Spencer, C. Fredrick, Q. Li, D. Westly, B. R. Ilic, B. Shen, M.-G. Suh, K. Y. Yang, C. Johnson, D. M. S. Johnson, L. Hollberg, K. J. Vahala, K. Srinivasan, S. A. Diddams, J. Kitching, S. B. Papp, and M. T. Hummon, "Architecture for the photonic integration of an optical atomic clock," Optica **6**, 680–685 (2019).
37. T. Gissibl, S. Wagner, J. Sykora, M. Schmid, and H. Giessen, "Refractive index measurements of photo-resists for three-dimensional direct laser writing," Opt. Mater. Express **7**, 2293–2298 (2017).
38. S. Dottermusch, D. Busko, M. Langenhorst, U. W. Paetzold, and B. S. Richards, "Exposure-dependent refractive index of Nanoscribe IP-Dip photoresist layers," Opt. Lett. **44**, 29–32 (2019).
39. M. Schmid, D. Ludescher, and H. Giessen, "Optical properties of photoresists for femtosecond 3D printing: refractive index, extinction, luminescence-dose dependence, aging, heat treatment and comparison between 1-photon and 2-photon exposure," Opt. Mater. Express **9**, 4564–4577 (2019).
40. E. D. Lemma, F. Rizzi, T. Dattoma, B. Spagnolo, L. Sileo, A. Qualtieri, M. D. Vittorio, and F. Pisanello, "Mechanical Properties Tunability of Three-Dimensional Polymeric Structures in Two-Photon Lithography," IEEE Transactions on Nanotechnol. **16**, 23–31 (2017).
41. A. Bertoncini, C. Liberale, and C. Liberale, "3D printed waveguides based on photonic crystal fiber designs for complex fiber-end photonic devices," Optica **7**, 1487–1494 (2020).